



Greenhouse gas measurements over a 144 km open path in the Canary Islands

J. S. A. Brooke¹, P. F. Bernath^{1,2}, G. Kirchengast³, C. B. Thomas¹, J.-G. Wang¹, K. A. Tereszchuk¹, G. González Abad¹, R. J. Hargreaves¹, C. A. Beale¹, J. J. Harrison¹, S. Schweitzer³, V. Proschek³, P. A. Martin⁴, V. L. Kasyutich⁴, C. Gerbig⁵, O. Kolle⁵, and A. Loeschner⁶

¹Department of Chemistry, University of York, York, YO10 5DD, UK

²Department of Chemistry & Biochemistry, Old Dominion University, Norfolk, VA 23529, USA

³Wegener Center for Climate and Global Change and IGAM/Inst. of Physics, University of Graz, Brandhofgasse 5, 8010 Graz, Austria

⁴School of Chemical Engineering and Analytical Science, University of Manchester, Oxford Road, Manchester, M13 9PL, UK

⁵Biogeochemical Systems Department, MPI for Biogeochemistry, Hans-Knöll-Str. 10, 07745 Jena, Germany

⁶Earth Observation Future Mission (EOP-SFP), ESA/ESTEC, P.O. Box 299, 2200 AG, Noordwijk, The Netherlands

Correspondence to: J. S. A. Brooke (jsabrooke@gmail.com)

Received: 16 April 2012 – Published in Atmos. Meas. Tech. Discuss.: 4 May 2012

Revised: 4 September 2012 – Accepted: 5 September 2012 – Published: 27 September 2012

Abstract. A new technique for the satellite remote sensing of greenhouse gases in the atmosphere via the absorption of short-wave infrared laser signals transmitted between counter-rotating satellites in low Earth orbit has recently been proposed; this would enable the acquisition of a long-term, stable, global set of altitude-resolved concentration measurements. We present the first ground-based experimental demonstration of this new infrared-laser occultation method, in which the atmospheric absorption of CO₂ near 2.1 µm was measured over a ~ 144 km path length between two peaks in the Canary Islands (at an altitude of ~ 2.4 km), using relatively low power diode lasers (~ 4 to 10 mW). The retrieved CO₂ volume mixing ratio of 400 ppm (± 15 ppm) is consistent within experimental uncertainty with simultaneously recorded in situ validation measurements. We conclude that the new method has a sound basis for monitoring CO₂ in the free atmosphere; other greenhouse gases such as methane, nitrous oxide and water vapour can be monitored in the same way.

1 Introduction

Climate change is primarily driven by anthropogenic greenhouse gas emissions, with the largest positive radiative forcing contribution due to increasing levels of long-lived carbon dioxide (CO₂) in the atmosphere (Solomon et al., 2007). Atmospheric CO₂ is therefore monitored by in situ observations at ground stations and in aircraft as well as by remote sensing methods.

In situ measurements include numerous precise instruments on the ground, for example at Mauna Loa Observatory, Hawaii (Keeling et al., 1976; Komhyr et al., 1989); on tall towers, for example in Europe for the CHIOTTO project (Continuous High-precision Tall Tower Observations of greenhouse gases; Vermeulen et al., 2011) as well as in the US (Bakwin et al., 1998); and in aircraft, for example in the CARIBIC project (Civil Aircraft for the Regular Investigation of the atmosphere Based on an Instrument Container; Schuck et al., 2009), for calibration of the TC-CON (Total Carbon Column Observing Network; Wunch et al., 2010) and as part of the NACP network (North American Carbon Program; Crevoisier et al., 2006).

Remote sensing of column CO₂ is carried out from the ground using direct sunlight in the near-infrared in the

TCCON (Wunch et al., 2010); recently from low Earth orbit (LEO) using reflected sunlight, for example by SCIAMACHY (SCanning Imaging Absorption spectroMeter for Atmospheric ChartographY; Schneising et al., 2011) and GOSAT (Greenhouse gases Observing SATellite; Yoshida et al., 2011); and using thermal infrared emission, for example by AIRS and IASI. As a further fundamental advance, carbon cycle science would benefit from an accurate and long-term, stable, global set of altitude-resolved greenhouse gas measurements as recently proposed using an infrared laser occultation technique (Kirchengast and Schweitzer, 2011).

The short-wave infrared (SWIR) spectral region, in particular $2.0\text{ }\mu\text{m}$ to $2.5\text{ }\mu\text{m}$, is attractive for active remote sensing measurements because of the availability of high quality lasers and detectors in this region, which contains vibration-rotation absorption lines of many greenhouse gases and their isotopologues (e.g. H_2O , HDO , H_2^{18}O , CO_2 , $^{13}\text{CO}_2$, C^{18}OO , CH_4 , N_2O , O_3 , CO) (Kirchengast and Schweitzer, 2011). Natural background radiation is also low in the SWIR region because it lies between the thermal IR region at longer wavelengths, where radiation is emitted by the Earth, and the visible region at shorter wavelengths, where emitted sunlight peaks (Liou, 2002).

The application of the IR laser occultation technique to satellite remote sensing requires measurements to be taken in a limb geometry, with a laser source on one satellite and a detector on a second, resulting in atmospheric path lengths of several hundred kilometers. The laser radiation is absorbed by molecules in the atmosphere and is subject to a number of “broadband” effects, such as aerosol and Rayleigh scattering, atmospheric scintillation and cloud absorption, that have weaker wavelength dependence than sharp molecular absorption lines (Schweitzer et al., 2011a). The influence of these broadband effects can largely be cancelled by making a differential measurement with two laser beams: one tuned to the peak absorption of a suitable vibration-rotation line and the other to a nearby “reference” wavelength subject only to broadband effects (Kirchengast and Schweitzer, 2011). This concept is part of a satellite mission called ACCURATE (Kirchengast et al., 2010) that was proposed as an Earth Explorer Mission to the European Space Agency (ESA) and viewed by ESA evaluation panels to be of very high scientific value and meriting further studies.

2 Experiment

2.1 Location

The Canary Islands ($\sim 28^\circ\text{N}$, $\sim 15^\circ\text{W}$) is a Spanish archipelago located off the west coast of Africa. Due to the clear skies and dry climate, the astronomical “seeing” is very good at higher elevations, and so the islands offer an ideal site for long path atmospheric measurements (Fig. 1). There are several astronomical observatories on the Canaries, in-



Fig. 1. Illustration of the laser link between the Canary Islands La Palma and Tenerife (map area $\sim 28^\circ\text{N}$ to $\sim 29^\circ\text{N}$, $\sim 18^\circ\text{W}$ to $\sim 16^\circ\text{W}$). Image 2012 Google[©] 2012 TerraMetrics[©] and 2012 GRAFCAN[©].

cluding the Roque de los Muchachos Observatory (ORM) on La Palma and the Teide Observatory (OT) on Tenerife, both at altitudes of $\sim 2.4\text{ km}$. There is a clear line of sight between these two observatories, which has previously been used for quantum communication experiments (Ursin et al., 2007).

2.2 Design

The experiment consisted of two optical setups: a laser transmitter (Tx) close to the Nordic Optical Telescope (NOT) at the ORM, and a receiver (Rx) connected to ESA’s Optical Ground Station (OGS) telescope at the OT. At the NOT site, the Tx (Fig. 2a) was located in a parking area near the telescope building and the laser beam was transmitted through a commercial 15 cm Newtonian telescope (Celestron OmniXLT150), on which was mounted a sighting telescope. The 1 m OGS Cassegrain telescope was used to collect the incoming radiation, which was then passed to the Rx (Fig. 2b), installed near the Coudé focus.

Two SWIR regions were tested: $\sim 2.1\text{ }\mu\text{m}$ (mainly CO_2 absorption) and $\sim 2.3\text{ }\mu\text{m}$ (mainly CH_4 absorption), hereafter referred to as the CO_2 and CH_4 regions, respectively. Calculated transmittance spectra for these regions are shown in the Appendix Figs. A1 to A3. The absorption lines selected for ACCURATE (Kirchengast and Schweitzer, 2011; Kirchengast et al., 2010) had to be altered for this experiment as a result of the enhanced spectral congestion at $\sim 2.4\text{ km}$ altitude. Lines were selected (Appendix Table A1) so that their predicted absorptions over the 144 km path at the expected atmospheric concentrations and conditions were neither too small nor saturated (Harrison et al., 2011), and so that they did not overlap significantly with strong H_2O lines. Nearby reference regions with minimal absorption were also identified. Four tunable single-mode distributed feedback diode (DFB) lasers manufactured by nanoplus GmbH (see Fig. 2) with (~ 4 to $\sim 10\text{ mW}$) emitted power were used to scan within these regions: two devoted for use as CO_2 region lasers (L1 and L2), and two for the CH_4 region (L3 and L4). The emitted laser wavelength was tuned by adjusting the laser temperature and the applied current. Each laser is

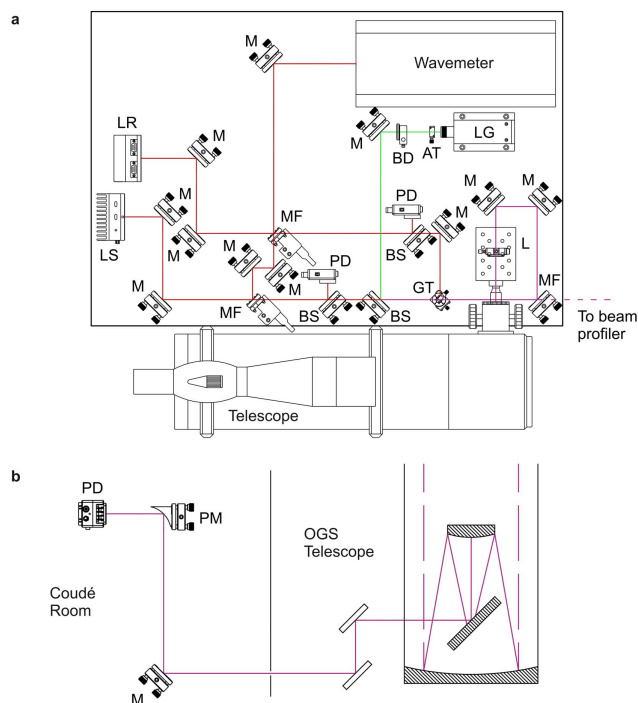


Fig. 2. Schematic diagram of the optical Tx and Rx breadboards. (a) Tx. (b) Rx. AT – neutral density filter to attenuate green laser (when necessary), BD – beam dump in motorized flipping mount, BS – dichroic beam splitter with transmission enhancing coating for ca. 2000 nm, GT – Glan-Thompson polarizing prism, L – CaF₂ lens (focal length = 10 mm), LG – frequency-doubled, Nd:YAG laser (200 mW, 532 nm). LR – IR diode laser 2 (serial number 592/21-24/nanoplus) or 4 (592/21-19/nanoplus), LS – IR diode laser 1 (264/3-9/nanoplus) or 3 (264/17-19/nanoplus), M – protected silver-coated mirrors with reflectivity of ca. 96 % at 2.1 μm , MF – silver-coated IR mirrors (M) in motorized flipping mount, PD – InGaAs photodiode detector, PM – gold-plated parabolic mirror, wavemeter – 1.0–5.0 μm wavemeter (Bristol Instruments 621-a).

tunable with high spectral resolution over a maximum spectral range of about 4 cm^{-1} (fine tuning) by adjusting the current, and about 10 cm^{-1} (coarse tuning) by adjusting the laser temperature. The half widths (HWHM) of the absorption lines at the expected average pressure of $\sim 780\text{ hPa}$ are $\sim 0.1\text{ cm}^{-1}$, and are easily resolved with the high spectral resolution of the lasers.

There were two lasers for each region, though only a single region was scanned at a time. Figure 2a illustrates the Tx setup for either region. The Tx breadboard was mounted on a stand with vertical and horizontal angle adjustments for laser alignment. The two lasers were linearly polarized at 90° to each other, so that the beams could be combined and overlapped with the polarizing beam splitter before being focused into the Tx telescope. Flip mirrors diverted the beams into the wavemeter before a scan to confirm the wavelength. During a scan, laser power was measured by extended InGaAs photodiode detectors (Thorlabs PDA10D),



Fig. 3. The laser beam hits the mountain side about 500 m away from the transmitter during collimation tests to calibrate the beam size as a function of lens (L in Fig. 2a) position.

to monitor the variation in power with wavelength and any other power fluctuations. The entrance lens of the telescope was adjusted to change the beam collimation produced by the telescope, thus enabling control of the beam size at the Rx. A green frequency doubled Nd:YAG laser (MGL-III-532-200mW-3 %) was used to assist in alignment on the Tx breadboard and with the receiver, utilizing its visibility and much higher power (200 mW). A scanning slit optical-IR beam profiler (Thorlabs BP109-IR2) was used to spatially overlap the green and the two IR lasers. This beam overlap, complemented by collimation tests of the green laser over a path of about 500 m (Fig. 3), was crucial to success.

At the Rx, the laser beam was collected by the 1 m OGS telescope, and sent through the optics (39 m focal length) to the Coudé room and thence through the simple Rx optics as shown in Fig. 2b. A parabolic mirror focused the divergent beam from the Coudé focus onto a thermoelectrically cooled extended InGaAs photodiode detector (Thorlabs PDA10DT). The IR laser power at exit of the Tx telescope was typically $\sim 3\text{ mW}$ to $\sim 5\text{ mW}$, and $\sim 1\text{ nW}$ to $\sim 100\text{ nW}$ was focused onto the Rx detector.

2.3 Measurement method

Spectra were recorded using a “fast scan” mode, in which an increasing ramp current was applied to the lasers to scan both broad ($\sim 3\text{--}4\text{ cm}^{-1}$) and narrow ($\sim 1\text{ cm}^{-1}$) microwindows for 4 s at 133 Hz and 400 Hz, respectively. The spectra were averaged over a 4 s interval to give a final spectrum. A series of 4 s periods was measured consecutively (typically for $\sim 20\text{ min}$), alternating between the two lasers L1 and L2 (or L3 and L4) every 4 s. The full data acquisition and processing procedure is described in Appendix A1 and A2.

In order to synchronize and time-stamp the detector data from the Tx and Rx, GPS timing units (NavSync CW46) with

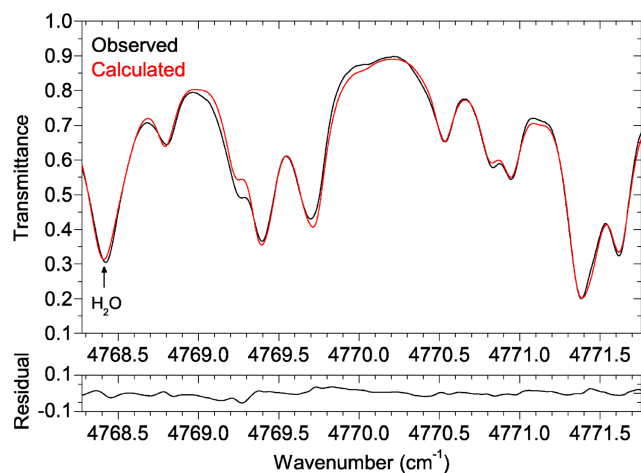


Fig. 4. Observed and calculated atmospheric transmittance spectra in the CO₂ region. All features arise from CO₂ absorption except for one, which is due to H₂O (labelled).

reported 30 ns accuracy were used. The GPS time signals were recorded simultaneously with those from the detectors.

2.4 Campaign

For the campaign, 11 measurement nights were available (11/12 to 21/22 July 2011). During tests at York it became apparent that daytime tests were impractical due to interfering sunlight. Unfortunately, the first week was plagued by calima, a weather phenomenon blowing dust over the Canaries from sandstorms in the Sahara desert, through which the beams could not pass due to strong aerosol extinction. When the calima cleared, the green beam could be seen by the operators at the Rx, so it could be guided into position using the Tx angle adjustments. This beam was so bright that it “lit up” the OGS building, and caused easily visible shadows. The first IR signals (for CH₄) were successfully detected during night 7 using a ~ 30 m beam diameter at the OGS.

Over the last few days of the campaign the wind speed increased, causing the transmitter, mounted outdoors, to shake slightly, so that beam movement became a problem. To compensate for this, the beam diameter was increased to ~ 100 m at the OGS so that part of the beam would always hit the Rx telescope. This decreased the received intensity, and the beam movement brought great intensity variations. It was however, with occasional adjustments of the beams, consistent enough to take measurements. Nights 10 and 11 were mostly spent successfully acquiring data in the CO₂ region. Some CH₄ region data were obtained at the end of night 11. Appendix Table A2 lists the scans performed.

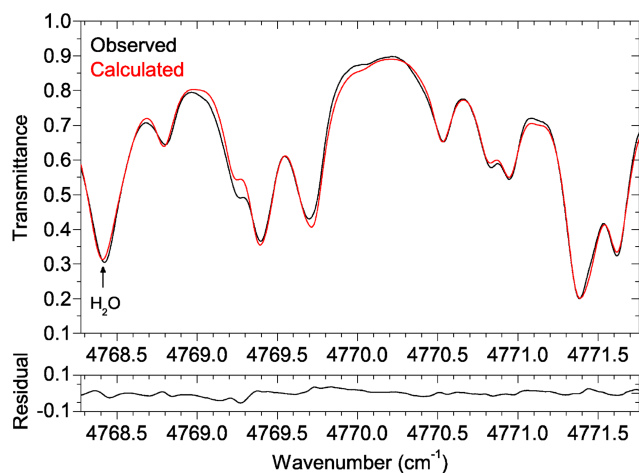


Fig. 5. Observed and calculated atmospheric transmittance spectra in the CH₄ region. All features arise from CH₄.

3 Results

During the campaign, the volume mixing ratios (VMRs) of CO₂, CH₄ and H₂O were recorded at 1 s intervals using two CRDS (cavity ring-down spectrometer) units for validation purposes (Picarro models G2401-m and 1301-m, at the Rx and Tx, respectively), complemented by routine meteorological station data both at the Rx and Tx. Here we present example data for CO₂ (Fig. 4). We retrieved an average CO₂ VMR ($400 \text{ ppm} \pm 15 \text{ ppm}$) along the line of sight, which we find in good agreement with the validation measurements as described below. A detailed data analysis will be published elsewhere. Additionally, a CH₄ spectrum covering the spectral region 4345.96 cm^{-1} to 4348.43 cm^{-1} (Appendix Table A2, label 12, laser L3) is presented (Fig. 5); however, the VMR cannot readily be retrieved due to equipment problems in the final hours of the campaign (see Appendix A5).

3.1 Fitting

For the full fitting procedure, see Appendix A3. The spectral region 4768.27 cm^{-1} to 4771.75 cm^{-1} was investigated (Appendix Table A2, label 7, laser L1), using the 4 s period of highest average signal intensity. A forward model based on the HITRAN 2008 line parameters (Rothman et al., 2009) and the line-by-line simulation procedure outlined by Rothman et al. (1998) was used to simulate and fit atmospheric transmittance spectra. A fit was performed, in which the simulation was repeated whilst altering several parameters, including CO₂ concentration, to minimize the residuals between the observed and calculated spectra; the resulting spectra are shown in Fig. 4. The final CO₂ concentration from this fit was taken as the result, yielding $400 \text{ ppm} (\pm 15 \text{ ppm})$, which is consistent with the validation value of $386.68 \text{ ppm} (\pm 0.21 \text{ ppm})$; see Appendix A4).

3.2 Error calculations

Atmospheric pressure and temperature along the beam path for the time of the investigated scan were modelled using the atmospheric analyses from ECMWF (European Centre for Medium-range Weather Forecasts). For both of these variables, the calculated full beam path values were adjusted based on the difference between their computed values at the start and end points, and those recorded by the local weather stations. The adjusted ray path values were then averaged, giving 285.2 K and 795.8 mbar. The standard deviations resulting from this averaging were used as error bars. The fitting procedure was repeated using the minimum pressure and temperature values calculated from the error bars, and again with the maximum values. The difference between the CO₂ concentration results from these extra fits and that from the main fit were 11.3 ppm and 10.7 ppm. The larger of the two was taken as the error caused by temperature and pressure uncertainties. The path length of 143.65 km was calculated using the recorded GPS coordinates.

The fitting procedure provides a final error covariance matrix, from which the standard deviation in the CO₂ concentration estimate was extracted. For the main fit, this value was 9.0 ppm. This was combined with the temperature and pressure error of 11.3 ppm and the detector offset error of 2.7 ppm (see Appendix A5) using the root sum squares method, yielding the final error of 15 ppm.

4 Discussion and conclusion

We have successfully demonstrated that atmospheric carbon dioxide concentrations can be determined from SWIR absorption measurements over very long path lengths, with relatively low power diode lasers (~ 4 to 10 mW). The accuracy of these demonstration measurements (± 15 ppm for CO₂) is limited by errors in determining the temperature and pressure along the atmospheric path length, uncertainties in the least-squares fitting procedure (partly due to low signal-to-noise ratio and errors in spectral line parameters – see below), and problems in the field associated with a detector offset error (see Appendix A5). The static link between the islands also does not demonstrate the scanning of the atmosphere which occurs between LEO satellites, and the experiment was too short to monitor trace gas variability over time. A detailed description of how the monitoring with the LEO system works is given by Kirchengast et al. (2010).

In general, the desired precision for remote sensing of CO₂ for carbon cycle science is about 1 ppm (Rayner and O'Brien, 2001); a detailed discussion of the observational requirements for the ACCURATE concept is available in Larsen et al. (2009), adopted by the mission proposal of Kirchengast et al. (2010). While the accuracy of this first demonstration experiment is not ideal, previous studies (Kirchengast and Schweitzer, 2011; Proschek et al., 2011) indicate that green-

house gas profiles for an ACCURATE mission are obtainable with < 1 to 4 % rms error (outside clouds; above 5 km; the goal for CO₂ is < 1 %). The sources of error contributing to the value of ± 15 ppm are expected to be significantly smaller for an ACCURATE mission than in this least-cost demonstration. The detector offset error is a fixable issue (see Appendix A5), and significantly more accurate frequency knowledge and higher signal-to-noise ratios will be available from advanced instrumentation. Furthermore, accurate temperature, pressure and humidity will be determined from simultaneous microwave occultation measurements (Kirchengast and Schweitzer, 2011; Schweitzer et al., 2011b), and a more accurate retrieval algorithm (Proschek et al., 2011) will be used to extract greenhouse gas concentrations from the infrared occultation measurements.

Implicit in the high accuracy of the ACCURATE mission is as well the requirement for accurate spectroscopic line parameters. Unfortunately, the accuracy of the line parameters presently available in the HITRAN database limits the accuracy of the demonstration measurements. For example, the CO₂ line intensities in the SWIR spectral region have reported errors in the range > 10 % and < 20 %. It is necessary to improve the HITRAN line parameters for the targeted absorption lines substantially in order for the ACCURATE mission to meet its accuracy goals (Harrison et al., 2011).

In summary, we conclude from this first experimental analysis that infrared laser occultation between LEO satellites (Kirchengast and Schweitzer, 2011) has a sound basis for monitoring CO₂ in the free atmosphere; other greenhouse gases such as methane, nitrous oxide and water vapour can be monitored in the same way. Further refined analysis of the Canary Islands campaign data is currently on-going, including for methane and water vapour in addition to CO₂, as well as preparations for more advanced instrumentation. This will enable a more stringent demonstration as a next step.

Appendix A

Supporting information

A1 Data acquisition and raw spectra

National Instruments (NI) data acquisition boards (analogue to digital/digital to analogue converters; ADCs) were used at both Tx and Rx locations (USB-6259 and USB-6251, respectively), and were controlled by custom written programs in NI LabVIEW 2010. These units are able to transform a digital input signal from a computer into an analogue voltage/current, and vice versa. At the Rx, this meant simultaneously recording the IR detector and GPS voltage signals, while at the Tx it also meant applying currents to the IR laser diodes. The ramp current was applied and the data sampled at 400 kHz (16 bits), with 1000 and 3000 samples per ramp (spectrum) for narrow and broad scans, respectively. These

Table A1. Selected absorption lines.

Absorption species	Wavenumber (cm^{-1})
$^{12}\text{CO}_2$	4772.657
$^{13}\text{CO}_2$	4766.641
C^{18}OO	4767.041
H_2O	4771.968
None (CO_2 region absorption minimum)	4770.150
CH_4	4348.166
None (CH_4 region absorption minimum)	4322.927

included 20 zero current samples at the start of the waveform to monitor offsets and drifts (see Appendix A5), followed by a rising linear ramp between two preset current values (typically ~ 40 mA to ~ 130 mA).

During a scanning session, the current ramp was continually applied to both lasers, as this helps stabilize the wavelength. Motorized flip mirrors were used to select automatically which laser beams were transmitted. Data were recorded in 4 s periods, hereafter referred to as repeats. The two IR lasers alternated for each repeat. Each ramp scanned the same current range, and therefore the same wavelength, producing 1600 or 533 spectra for each repeat for narrow and broad scans, respectively.

The GPS data added accurate timestamps to the detector data. The units had three outputs: data in ASCII format, analogue pulse per second signal (PPS), and an analogue 500 Hz square wave (FRQ). The PPS and FRQ signals were recorded by the ADC along with the detector signals. The data were output at 1 Hz, providing a timestamp. The PPS signal is a 1 Hz, 100 μs wide pulse, where the rising edge corresponds to the start of the next second. This enables a timestamp to be assigned to the data for the start of each second. The FRQ square wave enables timestamps to be assigned to the points in between. The timestamps at the Tx were corrected for the time taken for light to travel from the Tx to the Rx (479.3 μs).

The following procedure was applied to each 4 s repeat (recorded using one laser only) to obtain an averaged spectrum. There were two 4 s pieces of data: one from the Rx and one from the Tx. The detector offsets (measured every ~ 1 min; see Appendix A5) were first subtracted. The data of the Tx were interpolated to use the same timestamps as the Rx data so that each Rx data point can then be divided by its corresponding Tx point to correct for the smooth laser power change over wavelength, thus normalizing the data.

The points at which the ramp (spectrum) ends were found by observing when sudden drops in signal intensity occurred in the Tx data. The timestamps of these points were used to separate the individual spectra, which were then normalized to the one of highest average signal intensity, based on their means. They were then averaged in a weighted averaging process, in which the weight was based on the original

mean (before normalization) of the individual spectra, giving one final raw spectrum for a 4 s period. The weighted averaging process was used to account for the variation in signal intensity between individual spectra in one 4 s period, which is caused primarily by the wind shaking the Tx and by atmospheric scintillations.

A2 Wavelength calibration

A linear ramp current was applied to scan the laser, but the laser wavenumber is not a linear function of the applied current. The wavenumber axis was calibrated separately for each chosen scan range (Appendix Table A2). To achieve this, each scan was performed while the beam passed through etalons. This results in transmission fringes, with their peaks separated by the free spectral range (FSR) of the etalon.

To ensure that each scan covered the desired wavenumber range and therefore the selected absorption lines (Appendix Table A1), rough wavenumbers near the start and end of the scan were found using an etalon with an FSR much larger than the scan range, so that only one fringe is observed in one scan. A constant current near the end of the scan range was set, wavenumber recorded by the wavemeter, etalon angle set to maximum transmission, and scan performed. This showed one fringe where the scan sample number at maximum transmission corresponds to the recorded wavenumber. It was repeated for another constant current near the start of the scan range. The sample numbers at the two maximum transmissions were recorded (S1 and S2).

The relative wavenumber change was obtained accurately by scanning using a second etalon with an FSR of $\sim 0.0125 \text{ cm}^{-1}$. These fringes were fitted to quantify the change in wavelength with sample number. To create a preliminary wavelength axis, the results from the first etalon scans were used to give one absolute wavenumber point (at S2), and to estimate a value for the small FSR (by dividing the wavenumber difference between S1 and S2 by the number of small fringes in that range). The digital sample number can then be transformed into wavenumber. After the campaign, the final spectra were compared to those calculated by the forward model (GATS Spectralcalc; see <http://www.spectralcalc.com/>).

In all cases the spectra match extremely well, and there is minimal uncertainty in assigning peaks. For each scan type (see Appendix Table A2), a fit was then performed to minimize the residuals (observed-calculated) between the observed and calculated peak positions (using only CO_2 or CH_4 peaks) with the FSR and wavenumber offset as the only changing parameters. The profile of non-linearity of wavenumber with respect to digital sample number recorded by the second etalon was therefore still used in the calibration.

Table A2. Scans performed during the campaign.

Region	Label	Laser	Wavenumber range (cm ⁻¹)		Scan time (UTC)
			Start	End	
CO ₂	1	L1	4772.00	4772.84	Night 10
		L2	4768.03	4768.92	01:50–01:55
	2	L1	4770.97	4774.53	Night 10
		L2	4766.36	4768.18	02:23–02:30, 02:31–02:39, 02:41–02:43
	3	L1	4768.45	4769.34	Night 10
		L2	4765.32	4766.25	03:27–03:41
	4	L1	4768.24	4771.18	Night 10
		L2	4763.94	4768.21	04:32–05:04
	5	L1	4771.03	4771.86	Night 11
		L2	4768.55	4769.50	22:15–22:30, 22:37–22:44
CH ₄	6	L1	4770.35	4771.20	Night 11
		L2	4768.48	4769.42	22:59–23:00, 23:19–23:34
	7	L1	4768.27	4771.75	Night 11
		L2	4764.11	4768.20	00:14–00:33, 00:34–00:43
	8	L1	4770.91	4774.52	Night 11
		L2	4766.35	4768.19	00:54–01:13, 01:14–01:18
	9	L1	4773.81	4777.55	Night 11
		L2	4766.35	4768.19	01:31–01:38, 01:56–02:09
	10	L1	4771.17	4771.98	Night 11
		L2	4768.67	4769.60	02:55–03:09
	11	L3	4346.48	4347.39	Night 11
		L4	4321.57	4323.72	05:44–05:51
	12	L3	4345.96	4348.43	Night 11
		L4	4321.57	4323.72	06:21–06:38

A3 Floated fitting parameters

Four parameters were adjusted by the fitting program. Two were the VMRs of CO₂ and H₂O. The observed spectrum obtained from the procedure outlined above is in units of volts, which is effectively an arbitrary number, and the real position of the baseline is unknown. To be able to compare the spectrum to a calculated transmittance spectrum, it was necessary to use a multiplicative scaling factor. This scaling factor was the third fitting parameter, which was applied to the whole calculated spectrum after all other calculations. For the final presented spectra, the calculated and observed spectra are both divided by this parameter, to scale them to transmittance spectra. The laser radiation will have been subject to aerosol scattering, but with no wavelength dependence across the scan regions. The effects of this scattering are taken into account by this multiplicative factor, and will therefore have no noticeable effect on the final spectra.

The final fitting parameter was used to increase the broadening of the calculated spectrum from the theoretical values,

as the observed spectra are broader than the calculated ones (see Appendix A5). The spectra were fitted using Voigt line-shapes, a convolution of the Lorentzian and Gaussian line-shapes, resulting from a combination of mainly pressure-induced broadening and Doppler broadening, respectively. In the fit, the extent of pressure broadening was kept constant at the calculated level, and the multiplicative factor increased the influence of Gaussian broadening, effectively adding a Gaussian instrument function. The absorption peak areas, and thus concentrations, should not be influenced by the broadening caused by the limited detector bandwidth. The best broadening parameter from the fit was 1.31. The pressure, temperature and path length were kept constant in all the fits (see Appendix A5).

A4 CO₂ and H₂O VMR values

CO₂ is a well-mixed gas, and its VMR across the ray path is not expected to vary significantly. The validation CO₂ value reported is simply an average of the CRDS Rx and Tx values recorded at the time of the investigated scan. To estimate an

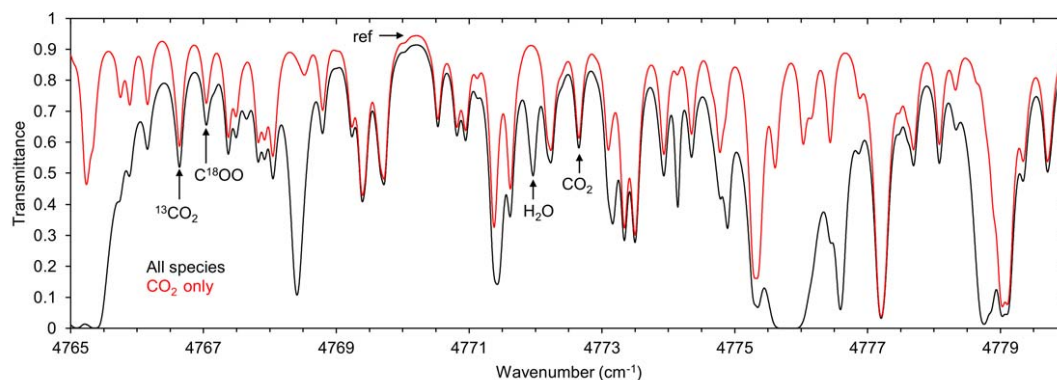


Fig. A1. Calculated spectrum of the CO₂ (2.1 μm) region. This shows the region covered by the two IR lasers for CO₂ and H₂O measurements (L1 and L2). CO₂ only – calculated for CO₂ only. All species – calculated including all relevant atmospheric species; almost all extra absorption is due to H₂O. The labels indicate the originally targeted absorption line positions and reference (minimum absorption) position (cf. Table A1). Depending on actual frequency scan ranges (cf. Table A2), other spectral sections are used. For conditions see Appendix A6.

error for this, the recorded CRDS CO₂ values for a ten minute period (five minutes either side of the actual scan time) from both the Tx and Rx were averaged, and the standard deviation was used as the error (± 0.18 ppm). This was combined with the reported error of the CRDS units (± 0.10 ppm) using the root sum squares method, giving the final validation error of ± 0.21 ppm. The VMR of H₂O across the beam path is likely to vary much more than that of CO₂, and so an actual average value could not be confidently calculated; therefore, its VMR was floated in the fitting process.

A5 Detector gain and offsets

It was necessary that the Rx detector used a high gain setting (~ 70 dB) due to the extent of power loss over the full path. The losses are primarily due to beam divergence, Rayleigh and aerosol scattering, and molecular absorption. This high gain limited the bandwidth of the detector so that the detector could not respond fast enough to rapid changes in laser power for the scan speeds used (400 kHz sampling rate). This has affected the observed spectra in two ways. Firstly, all of the spectra recorded on the campaign have broader peaks than expected from simulations, an effect that was not observed in prior studies in the laboratory when lower gain settings were used. Secondly, detector offsets (hereafter referred to only as offsets) were not measured as often as intended.

The original plan was to use 20 zero current samples at the start of each waveform so that an offset measurement could be taken regularly for each spectrum with zero laser power. This meant that any offset drift would be accounted for. The number of zero current samples used was kept small, as using more samples causes the laser wavelength not to respond as quickly to the applied current. This number of zero current samples was sufficient when using lower gain settings, but it was not satisfactory at higher gain settings. As a contingency, every ten 4 s repeats, a full repeat was recorded whilst both lasers were blocked, and the recorded values were averaged

to give an offset value for that repeat time. These provided the offsets for use in the data processing. For each repeat, the two closest (in time) recorded offset values were used to estimate an offset for the repeat, assuming a linear offset change between the two recorded times.

After the campaign, laboratory tests were performed to confirm that the gain setting and not the laser linewidth was the cause of the broadened peaks and offset problem. A gas cell was filled with CH₄, and spectra were recorded using both a high and a low gain setting. The laser power was reduced using several layers of tissue. These tests showed the expected extra broadening and lack of offsets using the high gain setting.

To estimate the error due to the offsets, all of the offsets recorded during the scanning session that contains the investigated repeat were averaged. The standard deviation was added to and subtracted from the actual offset used, and final spectra were calculated for each case. The fitting procedure was repeated, and the larger of the two differences between the calculated VMRs and the main VMR result was taken as the offset-caused error. An error of 2.7 ppm was estimated in this manner for the sample spectrum of Fig. 4.

To obtain a general idea of the possible effect of the offset variation on the repeats within a scanning session, it was quantified and normalized. The standard deviation of the recorded offsets was divided by the average received signal intensity. For the investigated CO₂ scanning session, this gave a variation of $\sim 1.0\%$. For the best CH₄ session, the estimated value is over 200%. The detailed reason for this high variation is currently unknown, but clearly there was a problem with the equipment when the CH₄ measurements were taken. For this reason, CH₄ spectra were not used in this study to retrieve concentrations, and the fit quality of the investigated CH₄ is significantly lower than that for CO₂. The underlying limitation is that CH₄ data could only be obtained in a short time at the end of the available measurement time;

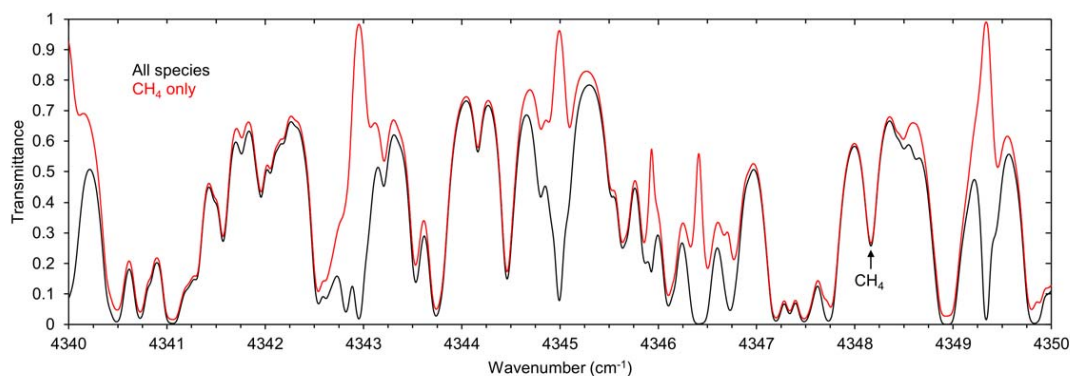


Fig. A2. Calculated spectrum of the CH₄ (2.3 μm) signal region. This region is covered by the IR laser for CH₄ measurements (L4). CH₄ only – calculated for CH₄ only. All species – calculated including all relevant atmospheric species; almost all extra absorption is due to H₂O. The label indicates the target absorption line position (cf. Table A1). Depending on actual frequency scan ranges, other spectral sections can be used. For conditions see Appendix A6.

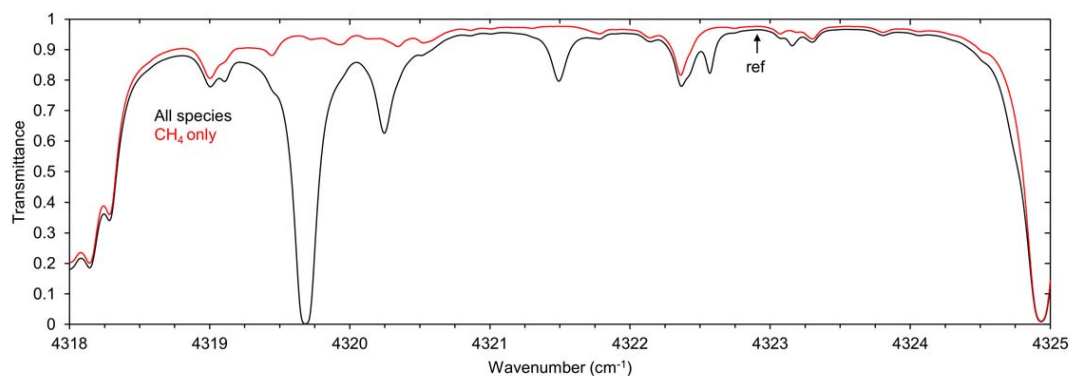


Fig. A3. Calculated spectrum of the CH₄ (2.3 μm) reference region. This region is covered by the IR laser for CH₄ reference measurements (L3). CH₄ only – calculated for CH₄ only. All species – calculated including all relevant atmospheric species; almost all extra absorption is due to H₂O. The label indicates the target reference (minimum absorption) position (cf. Table A1). Depending on actual frequency scan ranges, CH₄ might also be retrieved in this region. For conditions see Appendix A6.

if more time had been available, then better data could have been recorded.

A6 Conditions for calculated spectra

The spectra shown in Appendix Figs. A1 to A3 were calculated with the same forward model as was used in the fitting procedure, using the following conditions: altitude = 2.0 km and pressure = 795 hPa (to compensate for the varying altitude of the beam path due to the curvature of the Earth), temperature = 275.2 K, path length = 143.65 km, CO₂ VMR = 330 ppm, CH₄ VMR = 1700 ppb and H₂O VMR = 0.00463.

Acknowledgements. This research was funded by the European Space Agency's Support to Science Element (STSE) and supported by the Earth Observation Future Missions program, including the use of ESA's OGS facility. We thank the owners and operators of the NOT telescope for allowing us to use their facilities. We thank the Departments of Chemistry and Physics, University of York, for allowing us to test between their roofs. We also thank Gang Li and Nick Allen (York) for early background work, and Alex Brown (York) for help in making Figs. 4 and 5.

Edited by: J. Notholt

References

- Bakwin, P. S., Tans, P. P., Hurst, D. F., and Zhao, C. L.: Measurements of carbon dioxide on very tall towers: results of the NOAA/CMDL program, *Tellus B*, 50, 401–415, 1998.
- Chahine, M. T., Chen, L., Dimotakis, P., Jiang, X., Li, Q. B., Olsen, E. T., Pagano, T., Randerson, J., and Yung, Y. L.: Satellite remote sounding of mid-tropospheric CO₂, *Geophys. Res. Lett.*, 35, L17807, doi:10.1029/2008gl035022, 2008.
- Crevoisier, C., Gloor, M., Gloaguen, E., Horowitz, L. W., Sarmiento, J. L., Sweeney, C., and Tans, P. P.: A direct carbon budgeting approach to infer carbon sources and sinks. Design and synthetic application to complement the NACP observation network, *Tellus B*, 58, 366–375, doi:10.1111/j.1600-0889.2006.00214.x, 2006.
- Crevoisier, C., Chédin, A., Matsueda, H., Machida, T., Armante, R., and Scott, N. A.: First year of upper tropospheric integrated content of CO₂ from IASI hyperspectral infrared observations, *Atmos. Chem. Phys.*, 9, 4797–4810, doi:10.5194/acp-9-4797-2009, 2009.
- Harrison, J. J., Bernath, P. F., and Kirchengast, G.: Spectroscopic requirements for ACCURATE, a microwave and infrared-laser occultation satellite mission, *J. Quant. Spectrosc. Ra.*, 112, 2347–2354, doi:10.1016/j.jqsrt.2011.06.003, 2011.
- Keeling, C. D., Bacastow, R. B., Bainbridge, A. E., Ekdahl, C. A., Guenther, P. R., Waterman, L. S., and Chin, J. F. S.: Atmospheric Carbon-Dioxide Variations at Mauna-Loa Observatory, Hawaii, *Tellus*, 28, 538–551, 1976.
- Kirchengast, G. and Schweitzer, S.: Climate benchmark profiling of greenhouse gases and thermodynamic structure and wind from space, *Geophys. Res. Lett.*, 38, L13701, doi:10.1029/2011gl047617, 2011.
- Kirchengast, G., Bernath, P. F., Buehler, S., Durry, G., Facheris, L., Gerbig, C., Haimberger, L., Harris, J., Hauchecorne, A., Kurölä, E., Larsen, G. B., Sausen, R., Anthes, R. A., Gorbunov, M. E., Kursinski, E. R., Leroy, S. S., Trenberth, K., Randel, B., Gille, J., and Tsuda, T.: ACCURATE – climate benchmark profiling of greenhouse gases and thermodynamic variables and wind from space (ESA Earth Explorer Opportunity Mission EE-8 proposal), *Sci. Rep. No. 36*, document wcv-scirep-no36-gkirchengastetaljul2010.pdf, available at: <http://www.wegcenter.at/wcv/>, Wegener Center Verlag, Graz, Austria, 2010.
- Komhyr, W. D., Harris, T. B., Waterman, L. S., Chin, J. F. S., and Thoning, K. W.: Atmospheric Carbon-Dioxide at Mauna Loa Observatory, 1. NOAA Global Monitoring for Climatic-Change Measurements with a Nondispersive Infrared Analyzer, 1974–1985, *J. Geophys. Res.*, 94, 8533–8547, 1989.
- Larsen, G. B., Kirchengast, G., and Bernath, P. F.: Science objectives and observational requirements of the ACCURATE mission concept, *Tech. Rep. DMI/ESA IR-DAS/ObsReq/Oct2009*, available at: <http://due.esrin.esa.int/stse/files/project/131-176-149-94.201138102155.pdf>, Danish Meteorol. Inst., Copenhagen, Denmark, 2009.
- Liou, K. N.: An introduction to atmospheric radiation, 2nd Edn., Elsevier, San Diego, California, 2002.
- Proschek, V., Kirchengast, G., and Schweitzer, S.: Greenhouse gas profiling by infrared-laser and microwave occultation: retrieval algorithm and demonstration results from end-to-end simulations, *Atmos. Meas. Tech.*, 4, 2035–2058, doi:10.5194/amt-4-2035-2011, 2011.
- Rayner, P. J. and O'Brien, D. M.: The utility of remotely sensed CO₂ concentration data in surface source inversions, *Geophys. Res. Lett.*, 28, 175–178, doi:10.1029/2001GL013115, 2001.
- Rothman, L. S., Rinsland, C. P., Goldman, A., Massie, S. T., Edwards, D. P., Flaud, J. M., Perrin, A., Camy-Peyret, C., Dana, V., Mandin, J. Y., Schroeder, J., McCann, A., Gamache, R. R., Wattson, R. B., Yoshino, K., Chance, K. V., Jucks, K. W., Brown, L. R., Nemtchinov, V., and Varanasi, P.: The HITRAN molecular spectroscopic database and HAWKS (HITRAN Atmospheric Workstation): 1996 edition, *J. Quant. Spectrosc. Ra.*, 60, 665–710, 1998.
- Rothman, L. S., Gordon, I. E., Barbe, A., Benner, D. C., Bernath, P. F., Birk, M., Boudon, V., Brown, L. R., Campargue, A., Champion, J. P., Chance, K., Coudert, L. H., Dana, V., Devi, V. M., Fally, S., Flaud, J. M., Gamache, R. R., Goldman, A., Jacquemart, D., Kleiner, I., Lacome, N., Lafferty, W. J., Mandin, J. Y., Massie, S. T., Mikhailenko, S. N., Miller, C. E., Moazzen-Ahmadi, N., Naumenko, O. V., Nikitin, A. V., Orphal, J., Perevalov, V. I., Perrin, A., Predoi-Cross, A., Rinsland, C. P., Rotger, M., Simeckova, M., Smith, M. A. H., Sung, K., Tashkun, S. A., Tennyson, J., Toth, R. A., Vandaele, A. C., and Vander Auwera, J.: The HITRAN 2008 molecular spectroscopic database, *J. Quant. Spectrosc. Ra.*, 110, 533–572, doi:10.1016/j.jqsrt.2009.02.013, 2009.
- Schneising, O., Buchwitz, M., Reuter, M., Heymann, J., Bovensmann, H., and Burrows, J. P.: Long-term analysis of carbon dioxide and methane column-averaged mole fractions retrieved from SCIAMACHY, *Atmos. Chem. Phys.*, 11, 2863–2880, doi:10.5194/acp-11-2863-2011, 2011.
- Schuck, T. J., Brenninkmeijer, C. A. M., Slemr, F., Xueref-Remy, I., and Zahn, A.: Greenhouse gas analysis of air samples collected onboard the CARIBIC passenger aircraft, *Atmos. Meas. Tech.*, 2, 449–464, doi:10.5194/amt-2-449-2009, 2009.
- Schweitzer, S., Kirchengast, G., and Proschek, V.: Atmospheric influences on infrared-laser signals used for occultation measurements between Low Earth Orbit satellites, *Atmos. Meas. Tech.*, 4, 2273–2292, doi:10.5194/amt-4-2273-2011, 2011a.
- Schweitzer, S., Kirchengast, G., Schwaerz, M., Fritzer, J., and Gorbunov, M. E.: Thermodynamic state retrieval from microwave occultation data and performance analysis based on end-to-end simulations, *J. Geophys. Res.*, 116, D10301, doi:10.1029/2010jd014850, 2011b.
- Solomon, S., Qin, D., Manning, M., Chen, Z., Marquis, M., Averyt, K. B., Tignor, M., and Miller, H. L. (Eds.): *Climate change 2007: The physical science basis*, Contribution of Working Group I to the Fourth Assessment Report of the Intergovernmental Panel on Climate Change – IPCC, Cambridge University Press, 2007.
- Ursin, R., Tiefenbacher, F., Schmitt-Manderbach, T., Weier, H., Scheidl, T., Lindenthal, M., Blauensteiner, B., Jennewein, T., Perdignes, J., Trojek, P., Omer, B., Furst, M., Meyenburg, M., Rarity, J., Sodnik, Z., Barbieri, C., Weinfurter, H., and Zeilinger, A.: Entanglement-based quantum communication over 144 km, *Nat. Phys.*, 3, 481–486, doi:10.1038/Nphys629, 2007.
- Vermeulen, A. T., Hensen, A., Popa, M. E., van den Bulk, W. C. M., and Jongejan, P. A. C.: Greenhouse gas observations from Cabauw Tall Tower (1992–2010), *Atmos. Meas. Tech.*, 4, 617–644, doi:10.5194/amt-4-617-2011, 2011.

- Wunch, D., Toon, G. C., Wennberg, P. O., Wofsy, S. C., Stephens, B. B., Fischer, M. L., Uchino, O., Abshire, J. B., Bernath, P., Biraud, S. C., Blavier, J.-F. L., Boone, C., Bowman, K. P., Browell, E. V., Campos, T., Connor, B. J., Daube, B. C., Deutscher, N. M., Diao, M., Elkins, J. W., Gerbig, C., Gottlieb, E., Griffith, D. W. T., Hurst, D. F., Jiménez, R., Keppel-Aleks, G., Kort, E. A., Macatangay, R., Machida, T., Matsueda, H., Moore, F., Morino, I., Park, S., Robinson, J., Roehl, C. M., Sawa, Y., Sherlock, V., Sweeney, C., Tanaka, T., and Zondlo, M. A.: Calibration of the Total Carbon Column Observing Network using aircraft profile data, *Atmos. Meas. Tech.*, 3, 1351–1362, doi:10.5194/amt-3-1351-2010, 2010.
- Yoshida, Y., Ota, Y., Eguchi, N., Kikuchi, N., Nobuta, K., Tran, H., Morino, I., and Yokota, T.: Retrieval algorithm for CO₂ and CH₄ column abundances from short-wavelength infrared spectral observations by the Greenhouse gases observing satellite, *Atmos. Meas. Tech.*, 4, 717–734, doi:10.5194/amt-4-717-2011, 2011.